

Semiconductor, topological semimetal, indirect semimetal, and topological Dirac semimetal phases of $\text{Ge}_{1-x}\text{Sn}_x$ alloys

H.-S. Lan,^{1,*} S. T. Chang,² and C. W. Liu^{1,3,4,†}

¹*Graduate Institute of Electronics Engineering and Department of Electrical Engineering, National Taiwan University, Taipei, Taiwan*

²*Department of Electrical Engineering, National Chung Hsing University, Taichung, Taiwan*

³*Graduate Institute of Photonics and Optoelectronics, National Taiwan University, Taipei, Taiwan*

⁴*National Nano Device Labs, Hsinchu, Taiwan*

(Dated: November 9, 2016)

Electronic structures of $\text{Ge}_{1-x}\text{Sn}_x$ alloys ($0 \leq x \leq 1$) are theoretically studied by nonlocal empirical pseudopotential method. For relaxed $\text{Ge}_{1-x}\text{Sn}_x$, a topological semimetal is found for $x > 41\%$ with gapless and band inversion at Γ point, while there is an indirect-direct bandgap transition at $x = 8.5\%$. For strained $\text{Ge}_{1-x}\text{Sn}_x$ on a Ge substrate, semimetals with a negative indirect bandgap appear for $x > 43\%$, and the strained $\text{Ge}_{1-x}\text{Sn}_x$ on Ge is always an indirect bandgap semiconductor for $x < 43\%$. With appropriate biaxial compressive strains, a topological Dirac semimetal is found with band inversion at Γ and one pair of Dirac cones along the $[001]$ direction.

PACS numbers: 71.15.m, 31.15.bu, 71.70.Fk, 71.22.+i

Gray tin ($\alpha\text{-Sn}$) is a topological semimetal (also referred to topological zero-gap semiconductor) due to its inverted Γ_7^- and Γ_8^+ band states at zone center in the reciprocal space.¹⁻³ GeSn alloys with the diamond structure have been attractive for light-emitting⁴⁻⁶ and electronics^{7,8} applications owing to the potential direct bandgap of GeSn alloys and small transport effective masses, respectively. The indirect-direct bandgap transition of relaxed GeSn (r-GeSn) alloys reportedly occurred at Sn content around 7–10%.^{4,9-12} A zero gap behavior was also reported for r-GeSn at the Sn content larger than $\sim 40\%$ based on band structure calculations by the tight-binding model¹³ and the density function theory¹⁴. Moreover, strained $\alpha\text{-Sn}$ as a topological insulator was theoretically studied to have an opening gap between the split Γ_8^+ band states (Γ_8^+ and Γ_8^{+*})^{3,15} at zone center. However, the Dirac semimetal¹⁶ with one pair of Dirac cones in the Γ -Z direction, such as Cd_3As_2 ,^{17,18} has not yet been examined in $\alpha\text{-Sn}$. The nonlocal empirical pseudopotential method (EPM) has been widely used for calculating the electronic band structures of SiGe¹⁹⁻²¹ and GeSn^{7,11,22} alloy systems using virtual crystal approximation (VCA). The pseudocharge density, ρ_{pseu} , calculated by the electronic wave function was used for determining the bonding characteristics of Ge²³ and $\alpha\text{-Sn}$ ²⁴. Noted that the Γ_7^- and Γ_8^+ band states at zone center are s -like (antibonding s orbitals) and p -like (bonding p orbitals), respectively, for both Ge and $\alpha\text{-Sn}$.²⁵ In this work, the phase transition from a semiconductor to a topological semimetal in r-GeSn alloys is investigated. This transition is determined from the corresponding wave functions of Γ_7^- and Γ_8^+ band states at zone center. For strained $\text{Ge}_{1-x}\text{Sn}_x$ (s- $\text{Ge}_{1-x}\text{Sn}_x$) alloys, three phases (semiconductor, indirect semimetal, and topological Dirac semimetal) are found depending on Sn content

and compressive strain level.

The one-electron pseudo-Hamiltonian derived from Ref. 26 has four terms of the kinetic energy, local pseudopotential form factors ($V_{\text{loc}}(q)$), nonlocal correction terms ($V_{\text{nloc}}(\vec{G}, \vec{G}')$), and spin-orbit interactions ($V_{\text{so}}(\vec{G}, \vec{G}')$). The $V_{\text{loc}}(q)$ versus reciprocal lattice vectors ($q = |G - G'|$) are presented by the expression^{19,27}

$$V_{\text{loc}}^i(q) = \frac{1}{\Omega^i} \frac{b_1^i(q^2 - b_2^i)}{\exp[b_3^i(q^2 - b_4^i)] + 1} \left(\frac{1}{2} \tanh\left(\frac{b_5^i - q^2}{b_6^i}\right) + \frac{1}{2} \right), \quad (1)$$

where Ω^i is the atomic volume and i denotes the Ge or Sn element. The parameters of b_1^i , b_2^i , b_3^i , and b_4^i are obtained by solving roots of a system of nonlinear equations with the values of $V_{\text{loc}}^i(q)$ at $q^2 = \{3, 4, 8, 11\} \times (2\pi/a_0^i)^2$. The lattice constants (a_0) at 0 K of Ge (5.652 Å) and Sn (6.482 Å) are calculated using the value at RT²⁸ and the corresponding thermal expansion coefficients²⁹. EPM parameters of $V_{\text{loc}}(q)$, spin-orbit interactions (ζ and μ), and a fast cut-off tanh part²⁷ (b_5^i and b_6^i) of Ge and $\alpha\text{-Sn}$ (Table I) are adopted from Refs. 20, 22, 30, and 31 with less than 6% adjustment to reach good agreement with the experimental bandgaps of Ge^{28,32} and $\alpha\text{-Sn}$ ³³⁻³⁵ at low temperature. The parameters of nonlocal correction terms are obtained from Ref. 26 and the number of element plane wave basis set $\{\vec{G}\}$ is 339. Details of the three terms (V_{loc} , V_{nloc} , and V_{so}) were reported comprehensively by theoretical works.^{11,19,20,26,30,31,36} Here, we describe the approaches to take into account both strain and alloy effects in these three terms. The terms of V_{loc} and V_{nloc} , and the parameter λ in the V_{so} of Ge-Sn alloy systems are obtained by VCA using the following formulas

$$V^{\text{Ge}_{1-x}\text{Sn}_x}(q) = (1-x) \frac{\Omega^{\text{Ge}}}{\Omega_{\text{S}}^{\text{Ge}_{1-x}\text{Sn}_x}} V^{\text{Ge}}(q) + x \frac{\Omega^{\text{Sn}}}{\Omega_{\text{S}}^{\text{Ge}_{1-x}\text{Sn}_x}} V^{\text{Sn}}(q), \quad (2)$$

both for V_{loc} and V_{nloc} .

$$\lambda^{\text{Ge}_{1-x}\text{Sn}_x}(K, K') = (1-x) \lambda^{\text{Ge}}(K, K') + x \lambda^{\text{Sn}}(K, K'). \quad (3)$$

* Corresponding author : huangsianglan@gmail.com

† Corresponding author : chee@cc.ee.ntu.tw

TABLE I. Pseudopotential parameters used for Ge and Sn. (Ref. 30).

Parameter	Ge	Sn
$V_{\text{loc}}(\sqrt{3})\text{(Ry)}$	-0.2351 ^a	-0.191
$V_{\text{loc}}(\sqrt{4})\text{(Ry)}$	-0.1572	-0.152
$V_{\text{loc}}(\sqrt{8})\text{(Ry)}$	0.0186 ^a	-0.008
$V_{\text{loc}}(\sqrt{11})\text{(Ry)}$	0.055 ^a	0.04
$\zeta(\text{\AA}^{-1})$	5.34	4.75
$\mu (10^{-4} \text{ Ry})$	9.4 ^b	22.5
b_5 (atomic units)	4.5 ^a	3.9 ^c
b_6 (atomic units)	0.3 ^a	0.3 ^c

^a Reference 31.

^b Reference 20.

^c Reference 22.

The $\{\vec{G}\}$ and the normalizing strained atomic volume Ω_s^i generated from the lattice vectors are considered in the Hamiltonian matrix²⁰ with the strain and alloy effects. The linear interpolation of elastic constants (C_{11} , C_{12} , and C_{44})³⁷ and a bowing of 0.047 \AA ³⁸ for the lattice constant of GeSn alloys are used.

The band structure of r-Ge_{0.65}Sn_{0.35} [Fig. 1(a)], a typical direct-gap semiconductor, owns the conduction band edge at zone center (Γ_7^- state) and the degenerate valence band edges (Γ_8^+ states for heavy hole and light hole bands) with bandgap of ~ 70 meV. However, the band structure of r-Ge_{0.55}Sn_{0.45} [Fig. 1 (b)] shows a gapless topological semimetal behavior with the degenerate Γ_8^+ states above the Γ_7^- state. The corresponding constant ρ_{pseu} contours around the two atoms in the unit cell of the band states of s -like Γ_7^- and p -like Γ_8^+ show the band inversion of r-Ge_{0.55}Sn_{0.45} as compared to r-Ge_{0.65}Sn_{0.35} [Fig. 1 (c) and (d)]. The band inversion is also referred to the topological behavior.

The calculated indirect bandgap ($E_{\text{gL}} = L_6^+ - \Gamma_8^+$), direct bandgap ($E_{\text{g}\Gamma} = \Gamma_7^- - \Gamma_8^+$), and $E_{\text{g}\Gamma} + \text{spin-orbit splitting} (\Delta_0)$ ($E_{\text{g}\Gamma} + \Delta_0 = \Gamma_7^- - \Gamma_7^+$) as a function of Sn content for r-Ge_{1-x}Sn_x are shown in Fig. 2. Our calculations agree well with the reported experimental data at low Sn content ($E_{\text{g}\Gamma}$ and $E_{\text{g}\Gamma} + \Delta_0$) near 0 K^{10,39} (not shown). The calculated bandgaps of α -Sn ($E_{\text{gL}} = 0.13$ eV, $E_{\text{g}\Gamma} = -0.43$ eV, and $\Delta_0 = 0.8$ eV) are also consistent with reported values ($E_{\text{gL}} = 0.12$ eV,^{33,35} $E_{\text{g}\Gamma} = -0.42$ eV,³⁴ and $\Delta_0 = 0.8$ eV³⁴). There is no experimental E_{gL} data of r-Ge_{1-x}Sn_x near 0 K reported in literature. $E_{\text{g}\Gamma}$ decreases faster than E_{gL} with increasing Sn content and this results in an indirect-direct bandgap transition around $x = 8.5\%$ for r-Ge_{1-x}Sn_x. For $x > 41\%$, the degenerate Γ_8^+ forms a gapless topological semimetal ($E_{\text{g}} = 0$ eV) with the band inversion that the s -like Γ_7^- falls below the two p -like Γ_8^+ states in energy, i.e., $\Gamma_7^- - \Gamma_8^+ \sim -25$ meV of r-Ge_{0.55}Sn_{0.45} [Fig. 1 (b)]. The energy differences $\Gamma_7^- - \Gamma_8^+$, $L_6^+ - \Gamma_8^+$, and $\Gamma_7^- - \Gamma_7^+$ in gapless r-Ge_{1-x}Sn_x alloys are also shown in Fig. 2 for comparison.

For thin s-Ge_{1-x}Sn_x layer pseudomorphically grown on a Ge (001) substrate, the phase transition in the band structure from semiconductor to indirect semimetal with

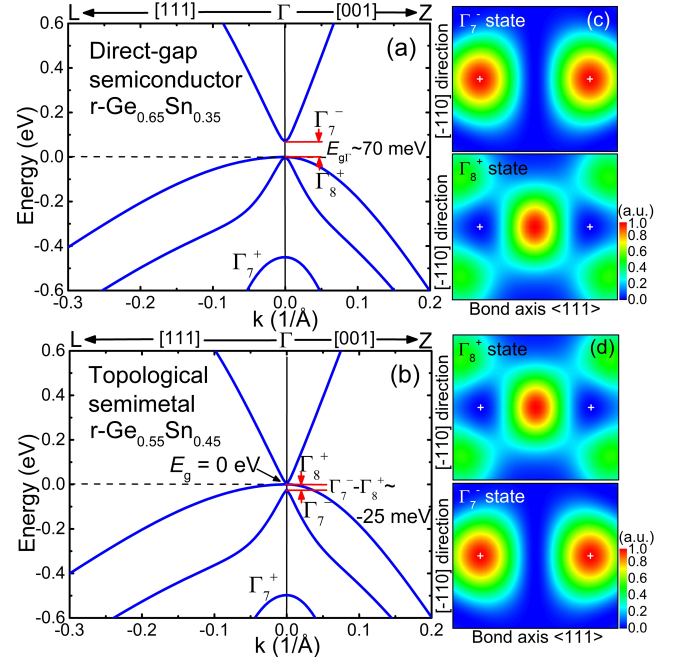


FIG. 1. The calculated band structures around zone center of (a) a direct-gap semiconductor (r-Ge_{0.65}Sn_{0.35}) and (b) a gapless topological semimetal (r-Ge_{0.55}Sn_{0.45}). The constant pseudocharge density (ρ_{pseu}) contours of the two atoms (indicated by +) in the unit cell of (c) r-Ge_{0.65}Sn_{0.35} and (d) r-Ge_{0.55}Sn_{0.45} to identify s -like Γ_7^- and p -like Γ_8^+ .

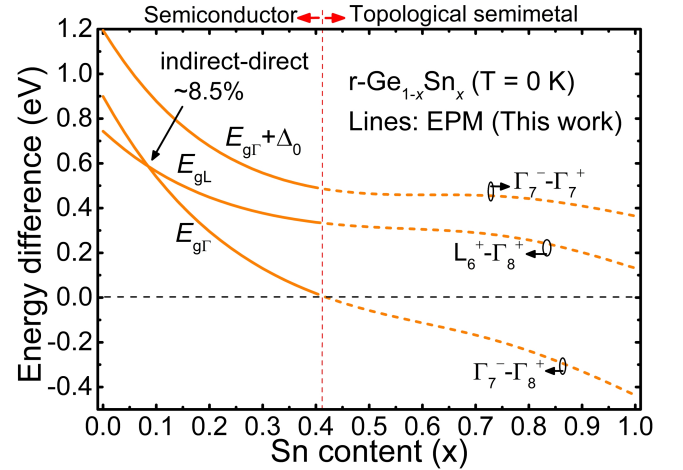


FIG. 2. The calculated energy differences of $\Gamma_7^- - \Gamma_8^+$, $L_6^+ - \Gamma_8^+$, and $\Gamma_7^- - \Gamma_7^+$ as a function of Sn content. The solid lines indicate the semiconductor bandgaps including E_{gL} , $E_{\text{g}\Gamma}$, and $E_{\text{g}\Gamma} + \Delta_0$, and the dashed lines ($x > 41\%$) indicate the energy differences of the topological semimetal.

the increase of Sn content is shown in Fig. 3. The s-Ge_{0.65}Sn_{0.35} on Ge [Fig. 3 (a)] has a typical indirect bandgap with conduction band edges at L_6^+ states and the valence band edge at Γ_8^+ state (the heavy hole band). For s-Ge_{0.55}Sn_{0.45} on Ge [Fig. 3 (b)], the L_6^+ states fall below the Γ_8^+ state, resulting in an indirect semimetal with a negative indirect bandgap ($L_6^+ - \Gamma_8^+ \sim -30$ meV). As

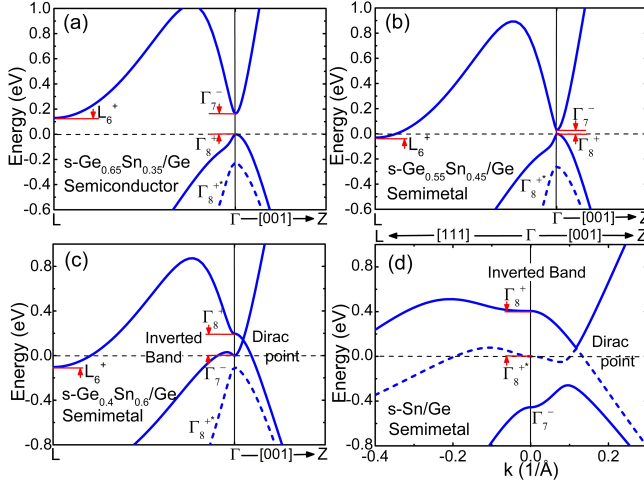


FIG. 3. Electronic band structures of $s\text{-Ge}_{1-x}\text{Sn}_x$ on Ge with different Sn content. (a) An indirect-gap semiconductor ($s\text{-Ge}_{0.65}\text{Sn}_{0.35}$ on Ge). (b) An indirect semimetal ($s\text{-Ge}_{0.55}\text{Sn}_{0.45}$ on Ge). (c) An indirect semimetal with the inverted band at zone center and a Dirac point along the [001] direction ($s\text{-Ge}_{0.4}\text{Sn}_{0.6}$). (d) An indirect semimetal with inverted band at zone center and a Dirac point along the [001] direction ($s\text{-Sn}$ on Ge). Note that the opening gap at zone center is $\Gamma_8^+-\Gamma_7^-$ and $\Gamma_8^+-\Gamma_8^{++}$ for (c) and (d), respectively.

Sn content reaches to 60% [Fig. 3 (c)], the band inversion of Γ_7^- and Γ_8^+ states occurs at zone center with an opening gap ($\Gamma_8^+-\Gamma_7^-$) at Γ point and a Dirac point along the [001] direction, but the L_6^+ states are still the conduction band edges. In this case, $s\text{-Ge}_{0.4}\text{Sn}_{0.6}$ on Ge is referred to an indirect semimetal with a negative indirect bandgap (not a topological Dirac semimetal). For $s\text{-Sn}$ on Ge in Fig. 3 (d), the large compressive strain ($\sim 12.8\%$) moves the Γ_8^{++} state upwards beyond the Γ_7^- state. However, conduction band edges remain at L_6^+ states. Moreover, the Dirac points are along [001] direction, not along [100] or [010] direction on the compressively strained plane, which is consistent with the previous report.¹⁵

Fig. 4 shows detailed phase transitions in $s\text{-Ge}_{1-x}\text{Sn}_x$ on Ge as a function of Sn content. The calculated energies, E_{gL} , $\Gamma_8^{++}-\Gamma_8^+$, and $\Gamma_7^+-\Gamma_8^+$, of $s\text{-Ge}_{1-x}\text{Sn}_x$ on Ge are consistent with reported experimental data^{40,41} at low Sn content (not shown). For $0 \leq x \leq 30\%$, $E_{g\Gamma}$ decreases faster than E_{gL} . As a result, the energy difference $E_{g\Gamma}-E_{gL}$ decreases with increasing Sn content. However, no crossover point is found because the increasing biaxial compressive strain with increasing Sn content moves the Γ_7^- state upwards as compared to the L_6^+ states, and thus the difference ($E_{g\Gamma}-E_{gL}$) increases again for $x > \sim 30\%$. An indirect semimetal with a negative indirect bandgap, $L_6^+-\Gamma_8^+$, occurs for $x > 43\%$. The band inversion at zone center is found for $x > 47\%$, and the opening gap at zone center changes from $\Gamma_8^+-\Gamma_7^-$ to $\Gamma_8^+-\Gamma_8^{++}$ at $x \sim 68\%$ due to the upward movement of Γ_8^{++} energy beyond the Γ_7^- state with increasing biaxial compressive strain.

In order to form a topological Dirac semimetal in $s\text{-Ge}_{1-x}\text{Sn}_x$, the biaxial compressive strain should be

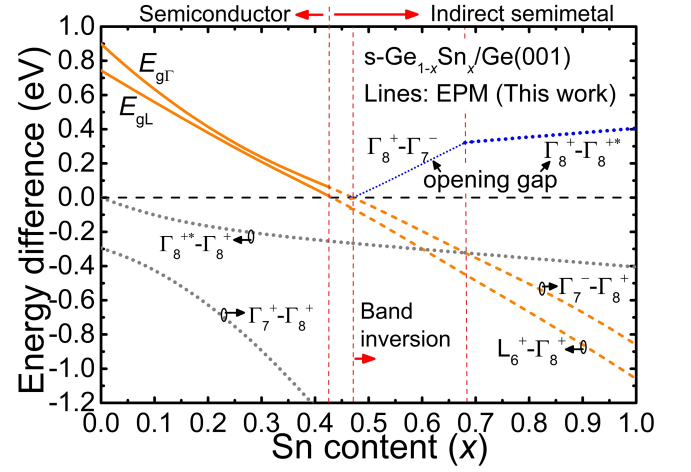


FIG. 4. The calculated energy differences of $\Gamma_7^+-\Gamma_8^+$, $L_6^+-\Gamma_8^+$, $\Gamma_8^{++}-\Gamma_8^+$, and $\Gamma_7^+-\Gamma_8^+$ of $s\text{-Ge}_{1-x}\text{Sn}_x$ on Ge as a function of Sn content. The semiconductor to indirect semimetal transition is found at $x > 43\%$ and the band inversion at zone center occurs at $x > 47\%$. The opening gap at zone center changes from $\Gamma_8^+-\Gamma_7^-$ to $\Gamma_8^+-\Gamma_8^{++}$ at $x \sim 68\%$.

smaller than that of $s\text{-Ge}_{1-x}\text{Sn}_x$ on Ge to make the energy of L_6^+ states in Fig. 3 (b) and (c) beyond the Γ_8^+ state. In the phase diagram defined by Sn content and biaxial compressive strain [Fig. 5 (a)], the semiconductor/topological Dirac semimetal transition for $s\text{-Ge}_{1-x}\text{Sn}_x$ is found in the Sn content range of 41–60% (the red line in Fig. 5 (a)). For semiconductor phase, the fundamental bandgap has three distinct regions for $E_{g\Delta x}$, E_{gL} , and $E_{g\Gamma}$. Note that the conduction band minima at Δ points are split into the 4 fold ($2\Delta_x$ and $2\Delta_y$) and 2 fold ($2\Delta_z$) valley degeneracies under biaxial compressive strain and the 4 fold has lower energy than the 2 fold. The band structures on the $k_{||}-k_z$ plane of $s\text{-Ge}_{0.4}\text{Sn}_{0.6}$ with the biaxial compressive strain ($\varepsilon_{||}$) of -0.5% and -3% show one pair of three-dimensional Dirac cones along the k_z direction [Fig. 5 (b) and (c)] and the band inversion at zone center. This is referred to as a topological Dirac semimetal, similar to the reported results of Cd_3As_2 .^{17,18} Note that the $k_{||}$ direction refers to the k_x [100] or k_y [010] axis perpendicular to the k_z [001] direction. The opening gap at zone center of topological Dirac semimetal changes from $\Gamma_8^+-\Gamma_8^{++}$ to $\Gamma_8^+-\Gamma_7^-$ (the white dash line in Fig. 5 (a)) with increasing biaxial compressive strain due to the Γ_7^- energy beyond the Γ_8^{++} state under high strain level.

Semiconductors with a direct or indirect bandgap, indirect semimetals with a negative indirect bandgap, topological semimetals, and topological Dirac semimetals are found in $\text{Ge}_{1-x}\text{Sn}_x$ alloy systems by band structure calculations using nonlocal EPM. The Sn content and strain level determine the phase of $\text{Ge}_{1-x}\text{Sn}_x$. The existence of diverse phases in $\text{Ge}_{1-x}\text{Sn}_x$ alloys has encouraged the exploration of possible applications of GeSn alloys.

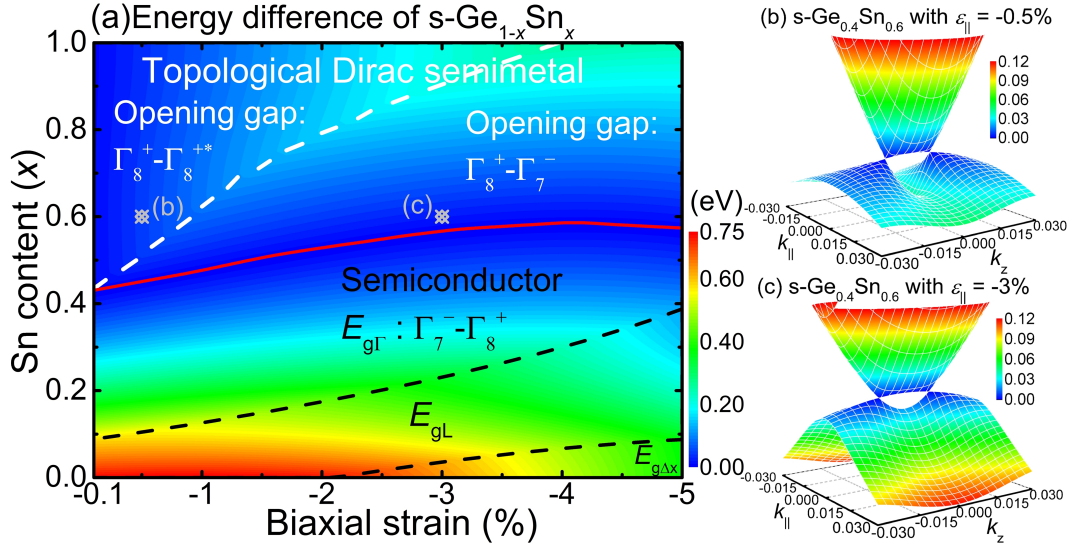


FIG. 5. (a) The phase diagram as a function of Sn content and biaxial compressive strain. The red line indicates the phase transition between direct-gap semiconductor and topological Dirac semimetal. The black dash lines distinguish the three regions for the fundamental bandgap ($E_{g\Delta x}$, E_{gL} , and $E_{g\Gamma}$) of semiconductor. The white dash line distinguishes the two regions for the opening gap ($\Gamma_8^+-\Gamma_8^{+*}$ and $\Gamma_8^+-\Gamma_7^-$) at zone center of topological Dirac semimetal. The band structure on the $k_{||}-k_z$ plane has one pair of three-dimensional Dirac cones located along the k_z direction for s-Ge_{0.4}Sn_{0.6} with (b) the biaxial compressive strain ($\epsilon_{||}$) of -0.5% and (c) the biaxial compressive strain ($\epsilon_{||}$) of -3%. The opening gap in (b) is $\Gamma_8^+-\Gamma_8^{+*}$, while the opening gap in (c) is $\Gamma_8^+-\Gamma_7^-$.

ACKNOWLEDGMENTS

This work was supported by Ministry of Science and Technology, Taiwan, R.O.C under Grant Nos. 105-2622-

8-002-001-, 105-2911-I-009-301, and 103-2221-E-002-232-MY3. The support of high-performance computing facilities by the Computer and Information Networking Center, National Taiwan University, is also highly appreciated.

- ¹ Hsin Lin, Tanmoy Das, Yung Jui Wang, L. A. Wray, S.-Y. Xu, M. Z. Hasan, and A. Bansil, Phys. Rev. B, **87**, 121202(R) (2013).
- ² Julien Vidal, Xiuwen Zhang, Vladan Stevanović, Jun-Wei Luo, and Alex Zunger, Phys. Rev. B, **86**, 075316 (2012).
- ³ Liang Fu and C. L. Kane, Phys. Rev. B, **76**, 045302 (2007).
- ⁴ S. Wirths, R. Geiger, N. von den Driesch, G. Mussler, T. Stoica, S. Mantl, Z. Ikonc, M. Luysberg, S. Chiussi, J. M. Hartmann, H. Sigg, J. Faist, D. Buca, and D. Grtzmacher, Nature Photon., **9**, 88 (2015).
- ⁵ H. S. Mczko, R. Kudrawiec, and M. Gladysiewicz, Sci. Rep., **6**, 34082 (2016).
- ⁶ Chung-Yi Lin, Chih-Hsiung Huang, Shih-Hsien Huang, Chih-Chiang Chang, C. W. Liu, Yi-Chiau Huang, Hua Chung, and Chong-Ping Chang, Appl. Phys. Lett., **109**, 091103 (2016).
- ⁷ H.-S. Lan and C. W. Liu, Appl. Phys. Lett., **104**, 192101 (2014).
- ⁸ Yee-Chia Yeo, Xiao Gong, Mark J. H. van Dal, Georgios Vellianitis, and Matthias Passlack, Tech. Dig.-Int. Electron Devices Meet. 2015, 2.4.1.
- ⁹ J. D. Gallagher, C. L. Senaratne, J. Kouvetakis, and J. Menéndez, Appl. Phys. Lett., **105**, 142102 (2014).
- ¹⁰ Vijay R. DCosta, Candi S. Cook, A. G. Birdwell, Chris L. Littler, Michael Canonico, Stefan Zollner, John Kouvetakis, and José Menéndez, Phys. Rev. B, **73**, 125207 (2006).
- ¹¹ Kain Lu Low, Yue Yang, Genquan Han, Weijun Fan, and Yee-Chia Yeo, J. Appl. Phys., **112**, 103715 (2012).
- ¹² F. L. Freitas, J. Furthmüller, F. Bechstedt, M. Marques, and L. K. Teles, Appl. Phys. Lett., **108**, 092101 (2016).
- ¹³ David W. Jenkins and John D. Dow, Phys. Rev. B, **36**, 7994 (1987).
- ¹⁴ Ming-Hsien Lee, Po-Liang Liu, Yung-An Hong, Yen-Ting Chou, Jia-Yang Hong, and Yu-Jin Siao, J. Appl. Phys., **113**, 063517 (2013).
- ¹⁵ A. Barfuss, L. Dudy, M. R. Scholz, H. Roth, P. Höpfner, C. Blumenstein, G. Landolt, J. H. Dil, N. C. Plumb, M. Radovic, A. Bostwick, E. Rotenberg, A. Fleszar, G. Bihlmayer, D. Wortmann, G. Li, W. Hanke, R. Claessen, and J. Schäfer, Phys. Rev. Lett., **111**, 157205 (2013).
- ¹⁶ Q. D. Gibson, L. M. Schoop, L. Muechler, L. S. Xie, M. Hirschberger, N. P. Ong, R. Car, and R. J. Cava, Phys. Rev. B, **91**, 205128 (2015).
- ¹⁷ Sangjun Jeon, Brian B. Zhou, Andras Gyenis, Benjamin E. Feldman, Itamar Kimchi, Andrew C. Potter, Quinn D. Gibson, Robert J. Cava, Ashvin Vishwanath, and Ali Yazdani, Nature materials, **13**, 851 (2014).
- ¹⁸ Madhab Neupane, Su-Yang Xu, Raman Sankar, Nasser Alidoust, Guang Bian, Chang Liu, Ilya Belopolski, Tay-

- Rong Chang, Horng-Tay Jeng, Hsin Lin, Arun Bansil, Fangcheng Chou, and M. Zahid Hasan, *Nature Communications*, **5**, 3786 (2014).
- ¹⁹ M. V. Fischetti and S. E. Laux, *J. Appl. Phys.*, **80**, 2235 (1996).
 - ²⁰ Martin M. Rieger and P. Vogl, *Phys. Rev. B*, **48**, 14276 (1993).
 - ²¹ P. Vogl, M. M. Rieger, J. A. Majewski, and G. Abstreiter, *Phys. Scr.*, **T49**, 476 (1993).
 - ²² Suyog Gupta, Blanka Magyari-Köpe, Yoshio Nishi, and Krishna C. Saraswat, *J. Appl. Phys.*, **113**, 073707 (2013).
 - ²³ John P. Walter and Marvin L. Cohen, *Phys. Rev. B*, **4**, 1877 (1971).
 - ²⁴ H. Aourag, B. Soudini, B. Khelifa, and A. Belaidi, *Phys. Stat. Sol. (b)*, **161**, 685-695 (1990).
 - ²⁵ P. Y. Yu and M. Cardona, *Fundamentals of Semiconductors*, 3rd ed. (Springer, Berlin, 2001).
 - ²⁶ James R. Chelikowsky and Marvin L. Cohen, *Phys. Rev. B*, **14**, 556 (1976).
 - ²⁷ P. Friedel, M. S. Hybertsen, and M. Schluter, *Phys. Rev. B*, **39**, 7974 (1989).
 - ²⁸ S. Adachi, *Properties of Group-IV, III-V and II-VI Semiconductors* (JohnWiley & Sons, 2005).
 - ²⁹ R. Roucka, Y.-Y. Fang, J. Kouvetakis, A. V. G. Chizmeshya, and J. Menéndez, *Phys. Rev. B*, **81**, 245214 (2010).
 - ³⁰ W. Potz and P. Vogl, *Phys. Rev. B*, **24**, 2025 (1981).
 - ³¹ Jiseok Kim and Massimo V. Fischetti, *J. Appl. Phys.*, **108**, 013710 (2010).
 - ³² Solomon Zwerdling, Benjamin Lax, Laura M. Roth, and Kenneth J. Button, *Phys. Rev.*, **114**, 80 (1959).
 - ³³ R. F. C. Farrow, D. S. Robertson, G. M. Williams, A. G. Cullis, G. R. Jones, I. M. Young, and P. N. J. Dennis, *J. Cryst. Growth*, **54**, 507 (1981).
 - ³⁴ T. Brudevoll, D. S. Citrin, M. Cardona, and N. E. Christensen, *Phys. Rev. B*, **48**, 8629 (1993).
 - ³⁵ R. J. Wagner and A. W. Ewald, *J. Phys. Chem. Solids*, **32**, 697 (1971).
 - ³⁶ Paul Harrison, *Quantum Well, Wires and Dots*, 2nd Edition (WILEY, 2005), p.373-379.
 - ³⁷ Guo-En Chang, Shu-Wei Chang, and Shun Lien Chuang, *IEEE J. Quantum Electron.*, **46**(12), 1813 (2010).
 - ³⁸ R. Beeler, R. Roucka, A. V. G. Chizmeshya, J. Kouvetakis, and J. Menendez, *Phys. Rev. B*, **84**, 035204 (2011).
 - ³⁹ H. Pérez Ladrón de Guevara, A. G. Rodríguez, H. Navarro-Contreras, and M. A. Vidal, *Appl. Phys. Lett.*, **91**, 161909 (2007).
 - ⁴⁰ D. Stange, S. Wirths, N. von den Driesch, G. Musler, T. Stoica, Z. Ikonc, J. M. Hartmann, S. Mantl, D. Grützmacher, and D. Buca, *ACS Photonics*, **2**, 1539 (2015).
 - ⁴¹ K. Zelazna, M. P. Polak, P. Scharoch, J. Serafinczuk, M. Gladysiewicz, J. Misiewicz, J. Dekoster, and R. Kudrawiec, *Appl. Phys. Lett.*, **106**, 142102 (2015).